Hindawi
Adsorption Science & Technology
Volume 2022, Article ID 3092941, 10 pages
https://doi.org/10.1155/2022/3092941

Research Article

Preparation and Energy Storage Performance of Perovskite Luminescent Materials by an Electrochemiluminescence Method

Dan Cheng, Zhaohai Yang, and Yilan Liang

Changchun Guanghua University, Jilin Changchun 130000, China

Correspondence should be addressed to Dan Cheng; chengdan@ghu.edu.cn

Received 23 August 2022; Accepted 16 September 2022; Published 3 October 2022

Academic Editor: Rabia Rehman

In recent years, metal halide perovskites have become attractive photosensitive materials due to their excellent optoelectronic properties. Due to its good characteristics, perovskites are used in solar photovoltaic power generation, light-emitting diodes, photodetectors, photocatalysis, and sensors and many other fields. Considering the wide application of perovskites and the study of potential bifunctional devices, the application of perovskites in energy storage devices is relatively small, and a small number of studies focus on organic-inorganic hybrid lead-halide perovskites. However, the related energy storage research on all-inorganic lead-halide perovskites with better stability, which has also been widely concerned, is very scarce. And nontoxic all-inorganic nonperovskite has zero research in energy storage. Based on the above situation, this paper selects the lead-free perovskite Cs2AgSbCl6, and two lead halide perovskites with different dimensions, -0-dimensional Cs4PbBr6 and 3-dimensional CsPbBr3, these three all-inorganic perovskites. It was for electrochemical performance testing.

1. Introduction

In the 1760s, the first industrial revolution, the use of coal, freed human beings and entered the age of steam [1]. In the 1870s, the second industrial revolution, the use of electricity and oil mainly generated by burning coal, enabled human beings to learn to convert mechanical energy into electrical energy and enter the electrical age [2]. In the 1940s and 1950s, the third scientific and technological revolution was an information control technology revolution mainly marked by the invention and application of atomic energy, electronic computers, space technology, and biological engineering. Going back to the source, the application of such technologies still cannot get rid of the consumption of nonrenewable resources [3]. Since the first industrial revolution, resources and energy have become an indispensable part of industrial upgrading and technological progress [4]. With the upgrading of technological revolution, energy consumption has become more and more serious [5].

As early as the second half of the 20th century, human beings gradually realized the serious harm caused by environmental pollution [6]. The unreasonable use of nonrenewable resources, greenhouse gases, and global climate problems is becoming more and more serious [7]. In addition, people are increasingly aware of the shrinking of fossil energy, and a new type of alternative energy is urgently needed [8]. Compared with the large-scale facilities that provide a large amount of electricity at present, the energy supply of new energy sources such as solar energy, tidal energy, biomass energy and geothermal energy is intermittent in nature [9]. At the same time, about 30 years ago, the world's first lithium-ion battery came into being [10]. In this regard, the research on this portable electronic device is still hot in academia and business today [11]. At present, driven by the fourth industrial revolution in the world, what follows is a new 21st century technology breakthrough mainly based on graphene [12]. At the same time, the application of these technologies puts forward higher requirements for energy storage devices [13].

Halogen perovskite materials are a new type of semiconductor optoelectronic materials developed rapidly in the past decade. Thanks to its excellent photoelectric properties, such as direct bandgap, tunable emission wavelength, wide spectral absorption, large optical absorption coefficient, high

carrier mobility, high fluorescence quantum yield, narrow emission spectrum, and high defect tolerance, halogen perovskite is widely used in the preparation of high-performance photovoltaic and photovoltaic devices, including applications in solar cells, light-emitting diodes, photodetectors, lasers, and other fields. Among them, the development in solar cells is most significant. The photoelectric conversion efficiency of perovskite solar cells has increased from the initial 3.8% to 252% after nearly a decade of research, which is close to the photoelectric conversion efficiency of single crystal silicon solar cells [14, 15]. The development and application of these devices are inseparable from the energy supply source [6]. Therefore, a stable, long-lasting energy supply device with excellent energy efficiency density and the combination of the above devices are in great demand [16].

Replacing conventional energy sources with fossil fuels, including lithium-ion batteries (LIB), solar cells (solar cells), supercapacitors (SC), nanogenerators (NG), biofuel cells (BFC), and photodetectors (PDs) [17], is therefore necessary to develop self-powered systems to meet the growing demand for long-term energy use in different environmental scenarios [18–20]. With the development of integrated power plant, small, light, high-density and high-reliability energy systems will be better combined [21–23]. For example, LIB and solar cell, if a new perovskite material with excellent photovoltaic effect is designed into an integrated dual-function device, it will have a broad development prospect in the future.

Electrochemiluminescence (ECL), also known as electrochemiluminescence, is the product of the combination of chemiluminescence and electrochemical methods. It refers to the luminescence phenomenon produced by the electrochemical method to produce some special substances and then further react between these electrogenerated substances or between electrogenerated substances and other substances. In addition to the advantages of chemiluminescence analysis such as high sensitivity, wide linear range, and simple device, electrochemiluminescence analysis can also overcome some shortcomings of chemiluminescence analysis, such as some chemiluminescence reagents which are not easy to preserve or unstable under specific conditions, it is difficult to control time and space, and it is difficult to reuse chemiluminescence reagents. And relatively poor reproducibility is caused by uneven solution mixing. Therefore, in recent years, electrochemiluminescence has attracted more and more attention.

In the context of new energy production capacity and energy storage, in the field of photovoltaics with production capacity, the emerging material-halide perovskites, which has received extensive attention, have also received widespread attention due to their excellent energy storage characteristics and maturity of technology. At the same time, due to the application of new perovskites in various fields, the charm of this material is also increased. Therefore, in order to give full play to the excellent performance of such halide perovskites, several representative all-inorganic halide perovskites with excellent photovoltaic performance were selected for lithium-ion batteries, and their lithium storage performance was studied and tested, and they were electrochemically modified to improve their energy storage performance. This has certain guiding significance for the development of perovskite multifunctional devices in the future.

In this paper, all-inorganic lead-free perovskite was applied to energy storage devices, and excellent electrochemical performance was obtained. And the modified all-inorganic lead-based perovskite material was also applied to lithium-ion batteries for the first time, achieving excellent electrochemical performance.

2. Materials and Methods

2.1. Overview of Perovskites. After the A or B position in standard perovskite is replaced or partially replaced by other metal ions, various composite oxides can be synthesized to form anionic defects or b-position ions with different valence states. It is a new type of functional materials with excellent performance and wide applications. Perovskite is a kind of ceramic oxide. The earliest discovery of this kind of oxide is the calcium titanate (CaTi03) compound existing in calcium titanium ore. At present, all the materials used are made artificially, so there is no problem of resource depletion. In addition, this kind of material is simple in process, and the cost can be greatly reduced. The commercial potential is unlimited. Furthermore, halide perovskites have attracted extensive attention as advanced photovoltaic materials due to the development of other photovoltaic devices.

In 1839, Russian mineralogist LA Perovski discovered "perovskites." The original perovskite is calcium titanate (CaTiO3) in perovskite. After development, with the blessing of condensed matter physics, perovskite is defined as having the same unit cell structure as CaTiO3, with the general formula ABX3 substance. The halogen element in the X position has been widely used in photovoltaics, and this perovskite is a new type of widely used perovskite. As a fast active material, it has excellent photoelectrochemical ones. Therefore, in addition to their wide application in photovoltaics, their excellent electrochemical properties enable new halide perovskites to be widely used (Figure 1), including lithium-emitting batteries, (LEDs) and solar energy storage devices. Halide perovskites are expected to be the focus of many applied researches in the near future. Due to the versatility of new perovskites, research in developing them into bifunctional materials is also emerging.

2.2. Introduction to the Structure of Perovskite Materials. Based on the discovery of a new mineral by German chemist and mineralogist Geologist Gustav Rose. In 1839, it was later proved that its composition was $CaTiO_3$. It was named perovskite to show the outstanding Russian mineralogist Count. Lev. Alexevichvon Perovski tribute. In addition to $CaTiO_3$, the common perovskite materials in nature include $SrTiO_3$, $PbTiO_3$, $NaNbO_3$, $Ca(Fe,Nb)O_3$, $MgSiO_3$, and $FeSiO_3$. In particular, two perovskites, $MgSiO_3$ and $FeSiO_3$, are the most abundant in the crust. Later, perovskite materials generally refer to a large class of substances that have the same crystal structure as $CaTiO_3$. Such materials can

Figure 1: Applications of perovskites in fields other than photovoltaics.

be represented by the general formula ABX3. In the typical structural unit of ABX3, the A cation occupies eight vertex angles, the B cation occupies the body center and the X anion occupies six face centers M1. B cations typically coordinate it. At present, the more mature halogen perovskite nanocrystalline materials mainly include organic/inorganic hybrid and all-inorganic perovskite materials based on lead and tin, and lead halide perovskite (LHP) is the main one, including $CH_3NH_3PbI_3$, $CH_3NH_3PbBr_3$, $CH_3NH_3PbCl_3$, $CsPbI_3$, $CsPbBr_3$, $CsPbCl_3$, and mixed halogen perovskite nanocrystals. Among them, the fluorescence quantum yield of colloidal solution of bromine-based $CH_3NH_3PbBr_3$ and $CsPbBr_3$ nanocrystals has reached nearly 100%.

The types of chemical bonds in perovskite compounds are usually ionic and covalent bonds, and the properties of such compounds vary with their crystal structure and symmetry. They show electrical, optical, and magnetic diversity and can act as insulators, ferroelectrics, semiconductors, superconductors, metallic conductors, and ionic conductors. Next, some important properties of perovskite compounds, including ionic conductivity, catalytic properties, ferroelectricity, and optoelectronic properties, are introduced in detail.

2.2.1. Ionic Conductivity. Ionic conductors are a class of materials with high ionic conductivity or diffusivity values. Their main functional feature is to allow ion migration while maintaining their own crystal structure stability. Ion conduction is a mechanism of current. In solids, ions usually occupy fixed positions in the lattice and do not move. However, ion conduction may occur, especially as the temperature increases. Materials exhibiting such characteristics are used for batteries. The well-known ionic conductive solids are β-Alumina ("base"), an alumina. When this ceramic is complexed with mobile ions such as Na^+, it behaves like a so-called fast ion conductor. The application of fast ionic conductors to solid electrolytes in electrochemical devices has recently attracted great interest, such as batteries, supercapacitors, sensors, and electrochromic windows. Generally, at room temperature, materials with ionic conductivity in the range of 10-4 to 10-1 cm can be regarded as superionic conductors. Some fast ionic conductors also exhibit significant electronic conductivity and are called mixed ionic electronic conductors.

2.2.2. Catalytic. Perovskite type composite metal oxides have the characteristics of conductivity, oxygen diffusion, oxygen permeability, oxygen uncertainty, and surface oxygen exchange performance. At high temperatures, such materials are mixed conductors of electrons or electron holes and oxygen ions. Doping of low valent metal ions leads to the emergence of oxygen holes. Their synergistic effect can achieve selective permeability to oxygen. They are used to prepare chemical reactors and membrane reactors with oxygen selectivity. Researchers from Tsukuba University in Japan found that ultraviolet light can regulate the transport of oxide ions in perovskite crystals at room temperature.

2.2.3. Optoelectronics. Understanding the fundamental properties of semiconductor materials, such as trap location and density, is critical to the design and application of semiconductor materials. Perovskite semiconductor materials are

electronically correlated systems, and their degrees of freedom such as charge, spin, orbit, and lattice are coupled and compete with each other. The electronic dimension will be semiconductors. Electronic dimension is defined as the connectivity of electron orbitals for electronic dimension which is superior to the conventional structural dimension for explaining the photovoltaic properties of all reported halide perovskites and other photovoltaic absorbers, such as band gap, carrier mobility, defect level, and device performance.

2.3. Preparation of All-Inorganic Perovskites. There are usually two methods: solution synthesis and coprecipitation. Chemical vapor deposition (CVD) is a method of depositing solid thin films from gaseous raw materials through chemical reactions. Since the prepared thin film can adhere closely to the substrate and has almost no dependence on the geometry of the substrate, changing the gas composition or deposition conditions (such as temperature and gas pressure) can change the chemical or physical properties of the film, and it is easy to control the thickness; CVD has been widely used in the process of material development. The CVD method is hindered by the high reaction temperature required for its synthesis scheme and the difficulty in engineering control of the morphology. The solution synthesis method can prepare uniform perovskite through a relatively simple operation scheme. Compared with a synthetic method, a coprecipitation method has the advantages of high safety and easy operation. The room temperature coprecipitation method can be divided into two types: ligand-assisted reprecipitation method and saturation method.

In general, in the ligand-assisted reprecipitation technique, firstly, the halide salt of the target perovskite (e.g., CsPbX3 corresponds to CsX, PbX2), is dissolved in a polar solvent (e.g., DMF, DMSO, isopropanol, and ethanol), and the ligand is added. After mixing oleylamine and oleic acid evenly, add to nonpolar solution-antisolvent (e.g., acetone and toluene). Alternatively, reprecipitation was performed using the same method by using Cs-oleate, a hydrohalic acid as a precursor. This synthesis has the characteristics of simple operation and mild synthesis conditions.

3. Results and Discussion

3.1. Principle of Energy Storage Technology. The standard capacity/energy experiment method is as follows:

(1) Allow the battery to adapt to the ambient temperature by standing at a specific temperature node

(2) Charge with a constant current and voltage of 12.5 A, and the cut-off current is 0.25 A

(3) Stand still

(4) Discharge lower at a current of 12.5 A

(5) Repeat steps (2)–(4) three times

The average capacity of three discharges in the standard capacity/energy experiment is recorded as C0, and the average discharge energy is recorded as W0, with C0 and W0 as the standard capacity and energy at this temperature node.

The energy and capacity released by the battery decrease with the decrease of temperature and the temperature dischargeable battery. The main reason is that the lower the temperature, the lower the activity of the chemical materials inside the battery, resistance of the battery, an increase in the voltage drop at the beginning and end of discharge, a decrease in the discharge platform voltage, and a shorter stable discharge duration. This results in a reduction in the available energy of the battery.

$$H_k = \frac{\partial g(x_k, u_k)/\partial x_k}{x_k} = x_k^{\wedge} = \left[-1 \frac{dU_{\mathrm{OCV}}}{dz}\right]. \tag{1}$$

H_k is the Jacobian matrix of the partial derivative of the state vector for the battery observation space equation. Specifically, in the process, lithium ions diffuse in the solid phase particles of the positive and negative electrodes and migrate in the electrolyte. Formula (3) is shown:

$$J = -D\frac{\partial c}{\partial x}, \tag{2}$$

$$J(x) = -D\frac{\partial c(x)}{\partial x} - \frac{F}{RT} Dc \frac{\partial \varphi(x)}{\partial x}. \tag{3}$$

J is the diffusion flux, φ is the potential of the electrode, and x is the position coordinate of the lithium ions.

T decreases, the diffusion coefficient D decreases, and the reaction current density of the electrode decreases, which is reflected as a decrease in the standard energy released by the battery. The result is shown in the following formula:

$$W(T) = 9.732 \times 10^{-6} T^4 - 4.396 \times 10^{-4} T^3. \tag{4}$$

In the formula, $W(T)$ is the standard energy of the battery at different temperatures, and T is the temperature.

3.2. Establishment of the Second-Order RC Equivalent Circuit Model. Common equivalent circuit models include first-order, second-order, and third-order to nth-order RC networks. The error of the first-order RC network model is large, and the accuracy of the second-order and third-order RC network models will be significantly improved. In addition, the higher the order of RC network, the better. When the order exceeds the fifth order, the model error will increase, and the computational complexity will further increase. Considering the accuracy and computational complexity of the model, the equivalent circuit model of the second-order RC network is selected in this paper.

Such terminal voltage U lithium iron phosphate is the most important external characteristic parameter. As shown in Figure 2, battery terminal voltage is not a constant value, and the voltage drops rapidly at the beginning and end of discharge, which has a close nonlinear relationship with the energy state of the battery. Therefore, there is a terminal voltage the battery for real-time prediction of the terminal voltage. It provides accurate input parameters for subsequent

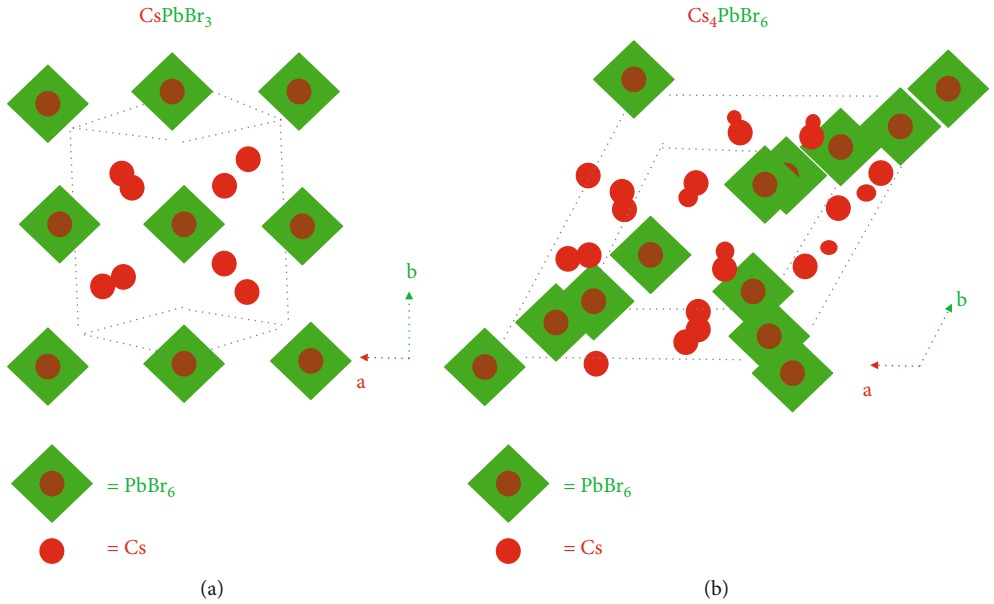

Figure 2: Second-order RC equivalent circuit model.

SOE estimation. As shown in Figure 2, considering that the parameter values will change with the change of temperature and SOE, the second-order RC is used to represent the terminal response characteristics under current excitation. The model includes two RC links, the current flowing through the resistor is the Faraday current, and the current flowing through the capacitor is the Faraday current. This polarization causes voltage relaxation phenomena, and the instantaneous polarization of the cell is approximated by resistance.

Output equations are shown in equations (5), (6), and (7):

(1) Equation of state:

$$\frac{dU_1}{dt} = -\frac{1}{R_1C_1}U_1 + \frac{1}{C_1}I, \tag{5}$$

$$\frac{dU_2}{dt} = -\frac{1}{R_2C_2}U_2 + \frac{1}{C_2}I. \tag{6}$$

(2) Output equation:

$$U = U_{OCV} - IR_0 - U_1 - U_2. \tag{7}$$

In the formula, U_{OCV} is the open-circuit voltage value of the battery when there is no current flowing, and R_0, R_1, and R_2 and C_1 and C_2 are the electrochemical and concentration polarized capacitors. U_1 is the voltage across the first *RC* loop, U_2 is the voltage across the second *RC* loop, and U is the terminal voltage of the battery.

3.3. Model Parameter Identification. The parameters to be identified in the second-order RC model include capacitors C_1 and C_2 and the time constants $\tau 1$ and $\tau 2$ of the two RC loops. Model parameter identification adopts HPPC (Hybrid Pulse Power Characteristic, HPPC) experiment. HPPC is a composite pulse power characteristic experiment recommended in the American Electric Vehicle Power Battery Testing Manual, and the battery internal resistance can be determined according to the battery's voltage response curve. The steps of the HPPC experiment are as follows:

(1) Allow the battery to adapt to the ambient temperature by standing at a specific temperature node

(2) Fully charge the battery with a constant current and voltage of 1 C_0

(3) Discharge with 1 C_0 current to discharge 10% of the standard capacity

(4) Let stand for 1 h

(5) Pulse experiments were carried out, firstly discharging with a constant 5 C_0 pulse current for 10 s, standing for 40 s, and then charging with a constant 5 C_0 pulse current for 10 s

(6) Repeat steps (3)–(5) until the final pulse experiment is performed at 90% depth of discharge (DOD)

(7) Discharge the battery to 100% DOD

(8) Let stand for 1 h

The current-voltage curve is a partial enlarged view of the pulse voltage response during the battery HPPC experiment. This figure is used the identification method of the model parameters.

First of all, the instantaneous voltage drop of *a-b* and the instantaneous voltage rise of *c-d* are caused by the ohmic internal resistance R_0, so

$$R_0 = \frac{(U_a - U_b/I) + (U_d - U_c/I)}{2}. \quad (8)$$

In the *d*-*e* stage, the current excitation $I = 0$, and the RC loop is in the zero input state.

$$U_i(t) = U_i(t_d)e^{-(t-t_d)/\tau_i}. \quad (9)$$

Among them, $U_i(t_d)$ is the terminal voltage of the *i*th RC loop at time td, τi is the time constant of the *i*th RC loop, $i = 1, 2$.At this time, the terminal voltage response of the circuit is

$$U(t) = U_{\mathrm{OCV}} - U_1(t_d)e^{-(t-t_d)/\tau_1} - U_2(t_d)e^{-(t-t_d)/\tau_2}. \quad (10)$$

U_{OCV} is the voltage at point *e* at the stationary end, and the values of parameters $U_i(t_d)$, and $\tau 1$ and $\tau 2$ can be obtained by least squares fitting. Point *a* is the end of the battery that has been left for a long time after the pulse, and it can be assumed that the internal polarization completely disappears at this time. The U_b to U_c stage is the zero-state response of the *RC* circuit.

$$R_i = \frac{U_i(t_c)}{I\left(1 - e^{-(t_c - t_a)/\tau_i}\right)}. \quad (11)$$

Among them, R_i represents the polarization internal resistance of the *i*-th *RC* loop, $i = 1, 2$. See the following formula:

$$C_i = \frac{\tau_i}{R_i}. \quad (12)$$

3.4. SOE Estimation Based on Sage-Husa EKF Algorithm. SOE represents the energy, which is defined as the ratio remaining energy of the battery to the standard energy, and its value ranges from 0 to 1. The released energy is the product integral of the voltage and the current. According to the above analysis, the standard energy is related to the temperature, and the expression for determining the SOE is shown in

$$Z_t = Z_0 - \frac{\int_0^t \eta(UI)dt}{W(T)}. \quad (13)$$

In the formula, z_t is the SOE state value of the battery at time *t*, z_0 is the initial value of the SOE state, $U\ W(T)$ standard energy of the battery at different temperatures.

The key of formula (13) lies in the calculation of the ratio of the product of terminal voltage and current to the battery energy, and the relationship between battery energy and temperature and between battery terminal voltage and SOE is nonlinear. Considering the aforementioned first part to establish the relationship between battery energy and temperature, the second part establishes the battery terminal voltage model at different temperatures and further considers formulas (4), (5), (6), and (13). The SOE estimation formula establishes the state equation and discretizes it, which can be expressed as

$$\begin{bmatrix} U_{1,k+1} \\ U_{2,k+1} \\ z_{k+1} \end{bmatrix} = \begin{bmatrix} 1 - \dfrac{\Delta t}{R_1 C_1} & 0 & 0 \\ 0 & 1 - \dfrac{\Delta t}{R_2 C_2} & 0 \\ 0 & 0 & 1 \end{bmatrix} \begin{bmatrix} U_{1,k} \\ U_{2,k} \\ z_k \end{bmatrix} + \begin{bmatrix} \dfrac{\Delta t}{C_1} \\ \dfrac{\Delta t}{C_2} \\ \dfrac{-U_k \Delta t}{W(T)} \end{bmatrix} I_k, \quad (14)$$

$$U_{k+1} = [-1, -1, 0] \begin{bmatrix} U_{1,k+1} \\ U_{2,k+1} \\ z_{k+1} \end{bmatrix} - I_{k+1}R_0 + U_{\mathrm{OCV}}. \quad (15)$$

U_k and U_{k+1} represent the terminal time k and the voltage at time $k + 1$ at both ends of the two *RC* loops, $U_{1,k}$ and $U_{2,k}$ represent the voltage at both ends of the two RC loops at time k, $zk + 1$ and zk are the SOE values of the battery at time $k + 1$ and time k, respectively, Δt is the sampling time interval of the system, R_0 is the ohmic internal resistance, R_1 and R_2 will be concentration polarization, C_1 and C_2 are the electrochemical, $W(T)$ is the standard energy at a certain temperature, I_k and I_{k+1} are the current time k and $k + 1$ time.

4. Experimental Results and Analysis

With the aim to explore the energy storage with the same high conversion efficiency and better stability, it was verified as such a bifunctional material combining energy storage and energy storage, due to the one, which makes CsPbBr3 the current all-inorganic perovskites.

4.1. Energy Storage Performance Analysis. The target monomer CsPbBr3 and its complex CsPbBr3@CNT were tested by, respectively, and the test results are shown in Figure 3. The XRD patterns of the monomer and the composite were found to be very similar, and both had good agreement with the standard card JCPDS: 18-0364. It should be noted that the bulging bulge around 2 Theta = 20° is caused by the diffraction of the glass substrate on which the sample tank is loaded. For the samples of the target monomer 3D CsPbBr3 and the composite CsPbBr3@CNT, the spectra were found to correspond to the peak positions of the monoclinic CsPbBr3 calibration card (JCPDS: 18-0364), and the peak intensity ratio was also related to the standard card. Similarly, no impurity peaks appeared, indicating that pure CsPbBr3 crystals were synthesized by the anti-solvent method without ligand assistance. The reason why the diffraction peaks of the CNT conductive matrix in the composite CsPbBr3@CNT are not shown in the spectrum is the same as that of the 0-dimensional perovskite Cs4PbBr6 composite, due to the lower composite ratio of CNTs (7%), and the degree of crystallinity as amorphous carbon is low.

Figure 4 shows the size distribution of CsPbBr3, and its average size was obtained by randomly sampling the size of 100 particle samples and taking the average value. It can be seen from the figure that the size distribution of the

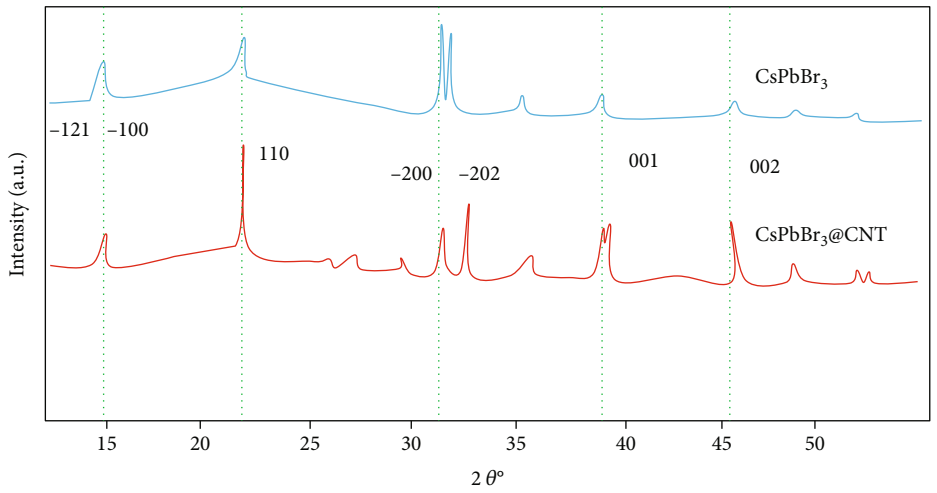

Figure 3: XRD patterns of CsPbBr3 and its composite CsPbBr3@CNT.

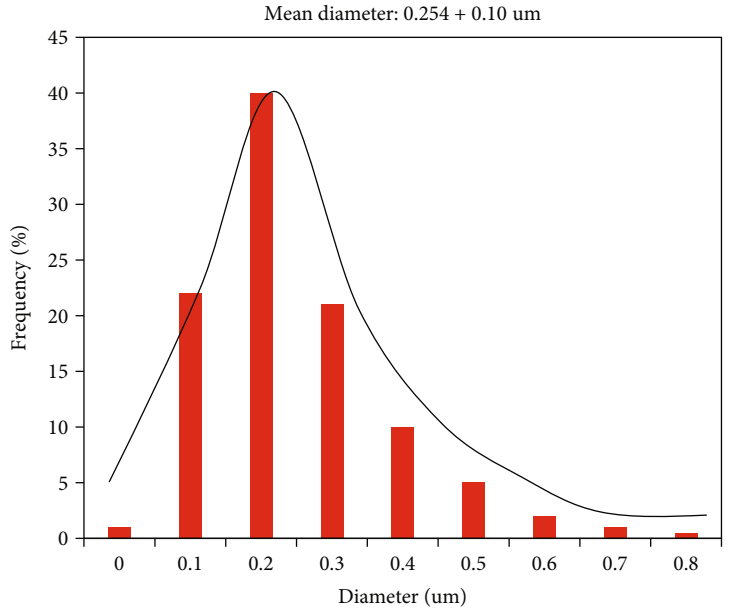

Figure 4: Size distribution of monomeric CsPbBr3.

monomer samples is relatively uniform, with an average size of 0.25 μm.

4.2. Analysis of Electrochemical Properties of Materials. The monomer CsPbBr3 and the composite CsPbBr3@CNT were used as the negative electrode active material, and the negative electrode material was mixed according to the ratio of active material : acetylene black : PVDF = 7 : 2 : 1, and the negative electrode material was coated on the current collector copper foil. The same steps were used to assemble a CR2032 button battery, and the electrochemical performance was tested under the same temperature and humidity conditions. The results of the test are as follows to compare their electrochemical performance.

Cyclic voltammetry testing of monomeric CsPbBr3 and composite CsPbBr3@CNT samples in a half-cell (vs. Li/Li +) with a scan rate of 0.5 mV s-1 and a voltage range of 0.01 V to 3.0 V for the first four turns. The scan spectrum is shown in Figure 5. In Figure 5(a), monomer Cs PbBr3 and (b) complex Cs PbBr3@CNT have very similar peak shapes—the spectrum shows four obvious oxidation peaks (0.6 V, 0.7 V, 1.9 V, and 2.4 V) and reduction peaks (2.7 V, 1.7 V, and 0.5 V)—this indicates that a similar electrochemical reaction occurs during the intercalation and migration of lithium ions in the negative electrode, and it is speculated that the lithium storage host is CsPbBr3. The scan images of the first circle and the second circle show different peak positions and peak shapes than the third and fourth scans, and the third and fourth circles almost coincide. Referring to the previous work of a large number of lithium battery negative electrodes, it can be seen that the SEI film was formed on the surface of the electrode due to the first scan. After that, the scanning images tended to be similar, also because the electrodes tended to be stable after the SEI film

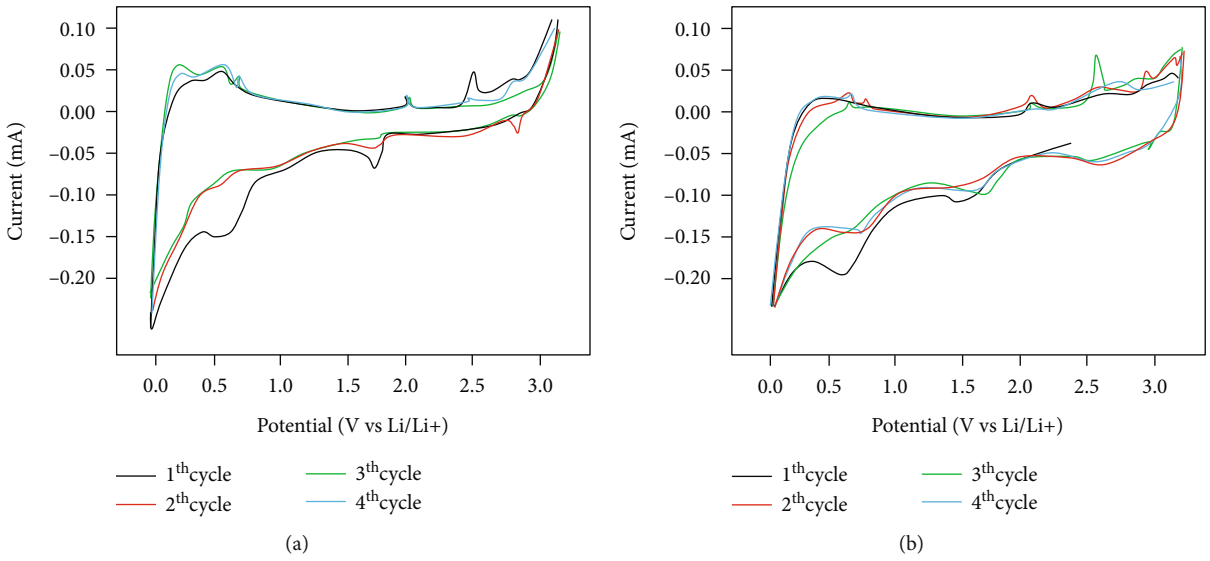

Figure 5: Cyclic voltammetry curves: (a) monomer Cs PbBr3; (b) complex Cs PbBr3@CNT.

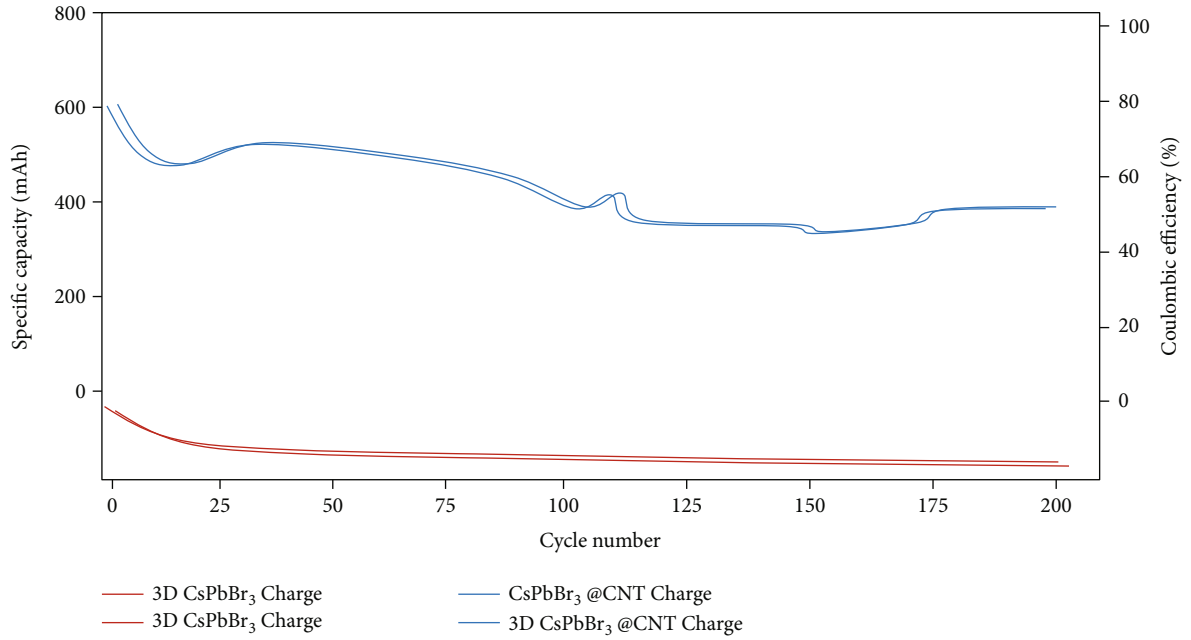

Figure 6: Galvanostatic charge-discharge (Coulombic efficiency) performance of monomeric CsPbBr3 and CsPbBr3@CNT composites.

was formed, and the electrochemical reactions were similar. Compared with the monomer cspbbr3, the C-V scan range of the complex CsPbBr3@CNT is larger, indicating that the composite CsPbBr3@CNT shows a larger lithium storage capacity, and the capacity decreases with the charge discharge cycle after the first scan. Therefore, it can be boldly speculated that the composite of carbon nanotubes enhances the electrochemical performance of CsPbBr3. Due to the lack of CV and mechanism analysis of the relevant literature, the electrochemical reactions on the relevant electrodes are still not very clear.

Figure 6 shows the relationship between the potential and the specific capacity with the charging and discharging process and the charge-discharge cycle diagram of the monomer CsPbBr3 at the current density of 100 mA g^{-1} under different cycle numbers, respectively. From the spectrum, the initial discharge capacity and charge capacity of the monomer are 130.7 mAh g^{-1} and 96.4 mAh g^{-1}, respectively. After 20 cycles, the capacity decays to about 50 mAh g^{-1}, and then, the capacity increases with the number of cycles. It remains in the decay state until it decays to 18.4 mAh g^{-1} after 200 cycles.

In order to further explore the electrochemical performance of 3D monomer CsPbBr3 and composite CsPbBr3@CNT as anodes for lithium ion batteries, the two materials were tested for their constant current charge-discharge performance in half cells, as shown in Figure 7.

In Figure 7, e charging capacities are 96.4 mAh g^{-1}, 87.5 mAh g^{-1}, 59.7 mAh g^{-1}, 47.7 mAh g^{-1}, and 24.4 mAh g^{-1},

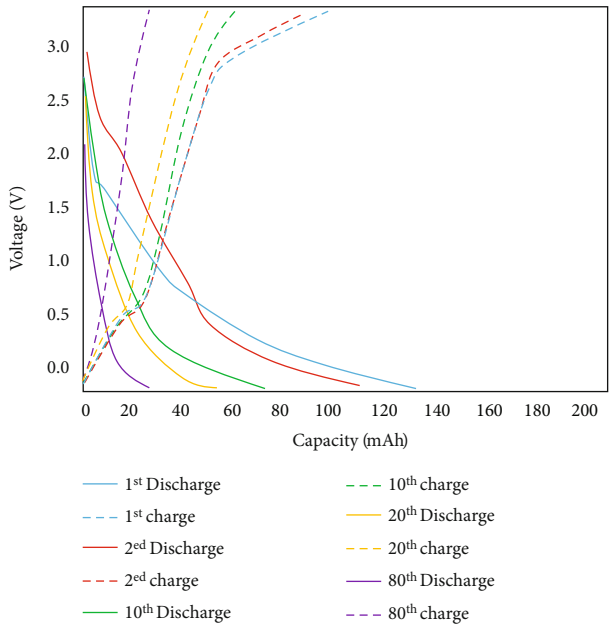

FIGURE 7: Voltage-specific capacity performance graphs of monomeric CsPbBr3 and CsPbBr3@CNT composites under different cycles.

and the capacity can be seen around 100 laps exhausted. The experimental data obtained in this work were obtained by Jiang et al. (102.6 mAh g^{-1}; 94.8 mAh g^{-1}) in the study of CsPbBr3 intercalation of lithium ions (first discharge and charge: that CsPbBr3 intercalates lithium ions through the lattice The expansion of the n-type doping, thereby relatively improving the conductivity of the perovskite.

5. Conclusion

Due to the lack of application of all-inorganic perovskites in energy storage devices, we synthesized Cs2AgSbCl6 under open conditions at room temperature by using an easy-to-operate experimental protocol (simplified non-ligand-assisted synergistic solvent reprecipitation reaction (CoLARP)), 0D Cs4PbBr6, and 3D CsPbBr3. Combined with the inherent poor electrical conductivity of perovskite and its instability in air, the composites Cs4PbBr6@CNT and CsPbBr3@CNT were obtained by combining the cesium lead bromide perovskite monomer with CNT with good electrical conductivity, respectively. The ratio of the negative electrode slurry was adjusted, and a button battery was assembled through the same steps. Under the same test conditions, relevant electrochemical tests were carried out and the electrochemical behavior during it was analyzed. This work is the first to apply CsPbBr3@CNT to Li-ion batteries, which is the first work in which a novel all-inorganic perovskite composite is applied to energy storage devices and exhibits electrochemical performance superior to that of commercial graphite anodes. The electrochemical performance exhibited by it has certain reference value in the material application of multifunctional devices in the future.

At present, environment-friendly and sustainable development promotes the research of lead-free halogen perovskite. We still need to make further efforts to prepare lead-free perovskite nanocrystals with high performance according to the existing practical experience and accumulated theoretical knowledge, and we hope that the prepared lead-free perovskite materials have certain application value.

Data Availability

The figures used to support the findings of this study are included in the article.

Conflicts of Interest

The authors declare that they have no conflicts of interest.

Acknowledgments

The authors would like to show sincere thanks to those techniques which have contributed to this research.

References

[1] M. K. Kim, Z. Munkhsaikhan, S. G. Han et al., "Structural engineering of single-crystal-like perovskite nanocrystals for ultrasensitive photodetector applications," *Journal of Materials Chemistry C*, vol. 10, no. 31, pp. 11401–11411, 2022.

[2] D. Meng, Q. Feng, M. Wang et al., "Realising high comprehensive energy storage performance of BaTiO 3-based perovskite ceramics via La(Zn 1/2 Hf 1/2)O 3 modification," *Ceramics International*, vol. 48, no. 11, pp. 16173–16182, 2022.

[3] S. Karabel Ocal, N. B. Kiremitler, A. F. Yazici, N. Celik, E. Mutlugun, and M. S. Onses, "Natural wax-stabilized perovskite nanocrystals as pen-on-paper inks and doughs," *ACS Applied Nano Materials*, vol. 5, no. 5, pp. 6201–6212, 2022.

[4] B. M. Bresolin, Y. Park, and D. W. Bahnemann, "Recent progresses on metal halide perovskite-based material as potential photocatalyst," *Catalysts*, vol. 10, no. 6, pp. 709–718, 2020.

[5] C. Matuszewska and L. Marciniak, "The influence of host material on NIR II and NIR III emitting Ni^{2+}-based luminescent thermometers in $ATiO_3$: Ni^{2+} (A = Sr, Ca, Mg, Ba) nanocrystals," *Journal of Luminescence*, vol. 223, no. 23, article 117221, 2020.

[6] P. Shukla, S. Yadav, M. S. Patel, P. Kumar, N. Kumar, and L. Kumar, "The effects of cesium lead bromide quantum dots on the performance of copper phthalocyanine-based organic field-effect transistors," *Nanotechnology*, vol. 32, no. 19, article 195208, 2021.

[7] Y. Liu, Z. Li, J. Xu et al., "Wide-bandgap perovskite quantum dots in perovskite matrix for sky-blue light-emitting diodes," *Journal of the American Chemical Society*, vol. 46, no. 5, pp. 1053–1061, 2022.

[8] C. Wu, H. Zhang, S. Wang, W. Wang, and J. Dai, "Room-temperature one-pot synthesis of highly stable SiO_2-coated Mn-doped all-inorganic perovskite $CsPb_{0.7}Mn_{0.3}Br_{0.75}Cl_{2.25}$ quantum dots for bright white light-emitting diodes," *Journal of Luminescence*, vol. 223, no. 5, article 117236, 2020.

[9] M. Chen, S. Hu, Z. Zhou et al., "Three-dimensional perovskite nanopixels for ultrahigh-resolution color displays and multilevel anticounterfeiting," *Nano Letters*, vol. 21, no. 12, pp. 5186–5194, 2021.

[10] S. Pal, A. Ghorai, D. K. Goswami, and S. K. Ray, "Strain mediated light emission using heterojunctions of all-inorganic mixed- halide perovskite nanocrystals via piezo-phototronic effect," *Nano Energy*, vol. 87, no. 2, article 106200, 2021.

[11] M. M. Baig, M. T. Mehran, R. Khan et al., "Direct chemical synthesis of interlaced NiMn-LDH nanosheets on LSTN perovskite decorated Ni foam for high-performance supercapacitors," *Surface and Coatings Technology*, vol. 421, no. 5686, pp. 127455–127972, 2021.

[12] M. Humayun, H. Ullah, M. Usman et al., "Perovskite-type lanthanum ferrite based photocatalysts: preparation, properties, and applications," *Journal of Energy Chemistry*, vol. 66, no. 7, pp. 314–338, 2021.

[13] M. Aramesh and B. Shabani, "Metal foam-phase change material composites for thermal energy storage: a review of performance parameters," *Renewable and Sustainable Energy Reviews*, vol. 155, no. 12, article 111919, 2022.

[14] S. M. Ferro, M. Wobben, and B. Ehrler, "Rare-earth quantum cutting in metal halide perovskites – a review," *Materials Horizons*, vol. 8, no. 4, pp. 1072–1083, 2021.

[15] K. Jger, P. Tillmann, E. A. Katz, and C. Becker, "Perovskite/silicon tandem solar cells: effect of luminescent coupling and bifaciality," *Solar RRL*, vol. 5, no. 3, article 2000628, 2021.

[16] B. K. Patra, H. Agrawal, J. Y. Zheng, X. Zha, A. Travesset, and E. C. Garnett, "Close-packed ultrasmooth self-assembled monolayer of CsPbBr3 perovskite nanocubes," *ACS Applied Materials & Interfaces*, vol. 12, no. 28, pp. 31764–31769, 2020.

[17] G. Guo, K. Ouyang, J. Yu, Y. Liu, S. Feng, and M. Wei, "Facile synthesis of LaCoO3with a high oxygen vacancy concentration by the plasma etching technique for high-performance oxygen ion intercalation pseudocapacitors," *ACS Applied Energy Materials*, vol. 3, no. 1, pp. 300–308, 2020.

[18] Q. Wu, X. Wu, Y. S. Zhao, and S. Zhao, "Design of lead-free films with high energy storage performance via inserting a single perovskite into $Bi_4Ti_3O_{12}$*," *Chinese Physics Letters*, vol. 37, no. 11, article 118401, 2020.

[19] Z. K. Hou, H. L. Cheng, S. W. Sun, J. Chen, D. Q. Qi, and Z. B. Liu, "Crack propagation and hydraulic fracturing in different lithologies," *Applied Geophysics*, vol. 16, no. 2, pp. 243–251, 2019.

[20] H. Cheng, D. Yang, C. Lu, Q. Qin, and D. Cadasse, "Intelligent oil production stratified water injection technology," *Wireless Communications and Mobile Computing*, vol. 2022, Article ID 3954446, 7 pages, 2022.

[21] H. Cheng, J. Wei, and Z. Cheng, "Study on sedimentary facies and reservoir characteristics of Paleogene sandstone in Yingmaili block, Tarim Basin," *Geofluids*, vol. 2022, Article ID 1445395, 14 pages, 2022.

[22] H. Cheng, P. Ma, G. Dong, S. Zhang, J. Wei, and Q. Qin, "Characteristics of carboniferous volcanic reservoirs in Beisantai Oilfield, Junggar Basin," *Mathematical Problems in Engineering*, vol. 2022, Article ID 7800630, 2022.

[23] Y. L. Chen, D. N. Yan, M. W. Zeng, C. S. Liao, and M. Q. Cai, "2D and 3D double perovskite with dimensionality-dependent optoelectronic properties: first-principle study on $Cs_2AgBiBr_6$ and $Cs_4AgBiBr_8$," *Journal of Physics: Condensed Matter*, vol. 34, no. 6, article 065501, 2022.